Generation of Perfect Cylindrical Vector Beams With Complete Control Over the Ring Width and Ring Diameter
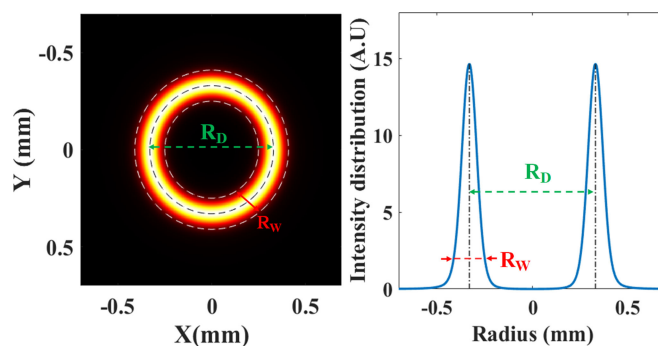
Prabin Pradhan, *Member, IEEE*
Manish Sharma
Bora Ung, *Senior Member, IEEE*

Generation of Perfect Cylindrical Vector Beams With Complete Control Over the Ring Width and Ring Diameter

Prabin Pradhan [ORCID] **, *Member, IEEE*, Manish Sharma, and Bora Ung** [ORCID] **, *Senior Member, IEEE***

Department of Electrical Engineering, École de technologie supérieure, Montreal, QC H3C1K3, Canada

Abstract: We propose the generation of high-purity perfect cylindrical vector beams (PCVB) using the Fourier transformation of Bessel–Gauss vector beams. The demonstration of PCVBs is implemented via an interferometric method employing a spatial light modulator that allows a fully independent control of the ring diameter (R_D) and ring width (R_W) of the PCVB. The proposed scheme enables to generate different types of cylindrical vector beams with precise user-defined transverse dimensions. The dynamic control of the ring width, ring diameter, and the specific type of PCVBs desired is theoretically as well as experimentally demonstrated. The proposed experimental setup can not only be employed in the generation of arbitrary PCVB, but also in perfect vortex beams. The ability to generate fully tailorable cylindrical vector beams and vortex beams has implications for the efficient launch of exotic optical modes in specialty fibers, in the field of optical tweezers as well as for superresolution microscopy.

Index Terms: Cylindrical vector beams, optical vortices, spatial light modulator, polarization.

1. Introduction

There is a burgeoning transformation in the optics and photonics world, which so far had been driven by Gaussian light beams. Increasingly, scientists and engineers are finding new applications that benefit from a beam of light whose intensity profile takes the shape of a single doughnut ring [1]–[3]. In particular, the so-called *cylindrical vector beams* (CVBs) with radial and azimuthal distribution of polarization exhibit unique properties when focused, which provide distinctive light-matter interactions compared to conventional (Gaussian-like) beams with homogeneous polarization [4], [5]. For example, a radially polarized doughnut shaped beam enables a significantly improved imaging resolution by providing a symmetric and high numerical aperture focus [6], [7]. More recently, CVBs have shown to enhance the quality and control over the laser processing of materials [8]. Furthermore, CVBs have promising applications in optical micro-manipulation [9], super-resolution imaging [10]–[12] and fiber optic transmission of exotic optical states [13], [14]. These emerging applications of CVBs, both in free space optics as well as in fiber optics, have reached a threshold

where further developments will require a greater control over the precise intensity profiles of the CVBs.

Precise control over the ring diameter and ring width of vortex beams (i.e. beams carrying orbital angular momentum) was recently achieved through the generation of perfect vortex beams, as demonstrated by a number of research groups [3], [15]–[19]. These recent works report the ability to maintain the dimensions of the beam intensity pattern irrespective of their topological charge (l). Furthermore, the reported new class of perfect vector vortex beams have been demonstrated with tailorable ring diameter irrespective to the polarization order. Still to the best of our knowledge, the independent control of the ring diameter *and* ring width in perfect cylindrical vector beams (PCVB) has not yet been demonstrated in its entirety [20]–[23]. So far, efforts towards the generation of PCVBs that would enable one to fully tailor the intensity profile of the CVBs of interest have yielded PCVBs with tunable ring diameter only that were of limited purity [20], [22], [23] (showing either residual light intensity in the beams centre or significant intensity fringing) via a method of limited flexibility due to the use of static optical elements [22]. In this work, we demonstrate the generation of arbitrary PCVBs whose transverse intensity profile (i.e. ring width and ring diameter) can be independently and easily controlled via an iris and a diffractive phase mask implemented on a programmable spatial light modulator (SLM). The proposed method is highly adaptable as it can be used to generate any type of PCVB as well as any topological orders of perfect vortex beams, using the same experimental setup. Our experimental results are supported by a rigorous theoretical framework as well as full-vector finite-element simulations that are in agreement with theory and results.

2. Theory

Perfect cylindrical vector beams are here generated by the interference of two coherent sources: a left and a right circularly polarized beam stemming from the Fourier transformation of Bessel beams. The experimental formulation for the Fourier transform of an ideal Bessel function is not amenable in practice. Therefore the Fourier transformation of the closely related Bessel-Gauss beams has been widely used instead in experiments. The Bessel-Gauss beam equation is mathematically written as [24]

$$E_{BG}(\rho, \varphi) = J_l(k_r\rho) \exp(il\varphi) \exp\left(\frac{-\rho^2}{w_g^2}\right) \tag{1}$$

where (ρ, φ) are the polar coordinate system, J_l is the lth order Bessel function of the first kind, k_r is the radial wavevector, l is the topological charge of the optical beam and w_g denotes the beam waist of the input Gaussian beam used to form the Bessel-Gauss beam. In the case of the first circularly polarized Bessel-Gauss beam, the x and y E-field components transform into a vector field given by

$$\vec{E}_{BG1}(\rho, \varphi, t) = J_l(k_r\rho) \exp\left(\frac{-\rho^2}{w_g^2}\right) \begin{pmatrix} \exp(il\varphi)\cos(\omega t) \\ \exp(il\varphi)\sin(\omega t) \end{pmatrix} \tag{2}$$

Likewise, the second circularly polarized Bessel-Gauss beam of opposite handedness and topological charge (l) is written as

$$\vec{E}_{BG2}(\rho, \varphi, t) = J_l(k_r\rho) \exp\left(\frac{-\rho^2}{w_g^2}\right) \begin{pmatrix} \exp(-il\varphi)\cos(\omega t) \\ -\exp(-il\varphi)\sin(\omega t) \end{pmatrix} \tag{3}$$

The coherent superposition of these two opposite circularly polarized light beams thus yields a CVB with a Bessel-Gauss profile:

$$\vec{E}_{BG}(\rho, \varphi, t) = 2 \cdot J_l(k_r\rho) \exp\left(\frac{-\rho^2}{w_g^2}\right) \begin{pmatrix} \cos(l\varphi)\cos(\omega t) \\ \sin(l\varphi)\sin(\omega t) \end{pmatrix} \tag{4}$$
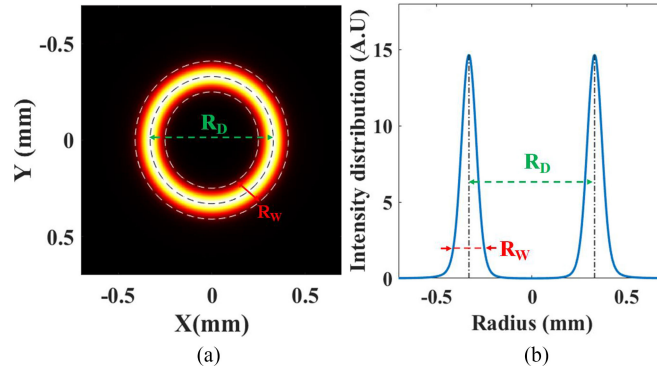
Fig. 1. (a) Finite-element simulation of a perfect cylindrical vector beam and its (b) radial intensity profile shown with ring width R_W and ring diameter R_D parameters

The latter CVB is passed through a Fourier lens transformation that converts the CVB into the desired PCVB, which can be written as

$$\vec{E}_{BG}(\rho, \varphi, t) = 2 \cdot i^{l-1} \frac{w_g}{w_o} \exp\left(-\frac{R^2 + R_r^2}{w_o^2}\right) I_l\left(\frac{2RR_r}{w_o^2}\right) \begin{pmatrix} \cos(l\theta + \phi)\cos(\omega t) \\ \sin(l\theta + \phi)\sin(\omega t) \end{pmatrix} \tag{5}$$

where $R = (\rho, \phi)$ is a shorthand notation for the polar coordinates, I_l is the lth order modified Bessel function of the first kind, ϕ is an offset phase added to tailor the relative phase between the two beams with opposite topological charges, and $R_W = 2w_o$ denotes the "ring width" of PCVB (as defined in Fig. 1) where $w_o = \frac{2f}{kw_g}$ is the beam waist of the input Gaussian beam at focus. The "ring radius" $R_r = \frac{R_D}{2}$ is governed by:

$$R_r = f \cdot \sin((n-1)\alpha) = \frac{k_r f}{k} \tag{6}$$

where n is the refractive index of the axicon material, α denotes the base angle of the axicon that is used to tune the ring radius of the PCVB, while $k = \sqrt{k_r^2 + k_z^2}$ and k_z respectively denote the total and longitudinal wavevectors. We note that a detailed description of the role and definition of the axicon parameter is given in Appendix A at the end of the paper. For large values of R_r at the Fourier plane, w_o becomes small and the modified Bessel function can be approximated as

$$I_l\left(\frac{2RR_r}{w_o^2}\right) = \exp\left(\frac{2RR_r}{w_o^2}\right) \tag{7}$$

Hence the expression of the Fourier-transformed CVB in (5) can be rewritten as

$$\vec{E}(R, \theta, t) = E_o \exp\left(-\frac{(R - R_r)^2}{w_o^2}\right) \begin{pmatrix} \cos(l\theta + \phi)\cos(\omega t) \\ \sin(l\theta + \phi)\sin(\omega t) \end{pmatrix} \tag{8}$$

where we defined $E_o = 2 \cdot i^{l-1} \frac{w_g}{w_o}$. Further, the propagating PCVB is written as

$$\vec{E}(R, \theta, z, t) = E_o \exp\left(-\frac{(R - R_r)^2}{w_o^2}\right) \exp\left(ikz - ik\left(\frac{R^2 + R_r^2}{2z}\right)\right) \begin{pmatrix} \cos(l\theta + \phi)\cos(\omega t) \\ \sin(l\theta + \phi)\sin(\omega t) \end{pmatrix} \tag{9}$$

Finally, when the above equation is evaluated at the focus of the Fourier lens ($z = f$) it simplifies as

$$\vec{E}(R, \theta, f, t) = E_1 \exp\left(-\frac{(R - R_r)^2}{w_o^2}\right) \exp\left(-ik\left(\frac{R^2 + R_r^2}{2f}\right)\right) \begin{pmatrix} \cos(l\theta + \phi)\cos(\omega t) \\ \sin(l\theta + \phi)\sin(\omega t) \end{pmatrix} \tag{10}$$

where $E_1 = E_o \exp(ikf)$. Equation (10) describes the complex E-field amplitude of the PCVB at the focal plane of the Fourier transform lens. This equation is useful for guiding the experimental
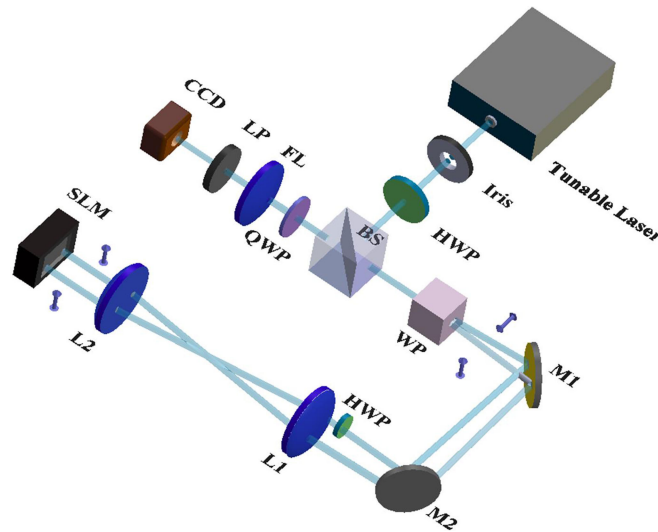
Fig. 2. Experimental setup for the generation of PCVB incorporating HWP: half wave plate, BS: beam splitter, WP: Wollaston prism, mirror (M1, M2), lenses (L1, L2), SLM: spatial light modulator, LP: linear polarizer, QWP: quarter-wave plate, FL-Fourier lens and variable iris diaphragm.

realization of PCVBs and to analyze the results. By controlling the input beam waist w_g one can tune the ring width (R_W) of the PCVB. Similarly, the ring diameter (R_D) can be independently controlled by varying the radial wavevector k_r that is related to the axicon parameter in (6) and (12).

3. Experimental Setup

The experimental setup for the generation of PCVB is based on a common-path interferometric scheme and a spatial light modulator (SLM), as is schematically depicted in Fig. 2. The linearly polarized input Gaussian beam from the tunable laser source at 1550 nm is collimated to a 3 mm diameter beam using an objective lens. This collimated beam is allowed to pass through an iris to adjust the incident beam diameter. A first half-wave plate (HWP) is placed before a 50:50 non-polarizing beam splitter (BS) to ensure that the linearly polarized beam is at a 45° angle with respect to the plane of incidence. The Wollaston prism (WP) splits the input Gaussian beam into two beams of vertical and horizontal polarizations diverging at an angle of 1.3°. The horizontally polarized beam subsequently passes through a second HWP to make it vertically polarized in order to match the polarization dependence of the phase-only SLM. Further, a two-lens arrangement (L1 and L2) is employed to collimate the diverging beams before they interact with the phase masks digitally imprinted on the SLM. A blazed grating phase mask was designed using a homemade Matlab script and numerically transferred to the SLM in real-time. Henceforth, the two back-diffracted beams from the reflective SLM travels back through the same arrangement of lenses and prisms so that they recombine into a single coherent beam. The interference of the two orthogonally linearly polarized beams with opposite topological charges results in the formation of a vectorial beam exhibiting spatially inhomogeneous polarization. The role of the quarter-wave plate (QWP) is to convert the two orthogonally linearly polarized beams into left and right circularly polarized beams, respectively. The generation of different types of CVBs actually depends on the relative phase difference (ϕ) imparted by the phase mask of the SLM. The Fourier lens (FL) transforms the field distribution of the diffracted beams so as to generate a single PCVB at the focus. Finally, a CCD camera captures the intensity profile of the generated PCVB.

4. Result and Discussion

The screen of the reflective phase-only SLM (1920 × 1152 pixels) was divided into two equal halves, each addressing a different incoming beam, so as to produce two 1st-order diffracted beams
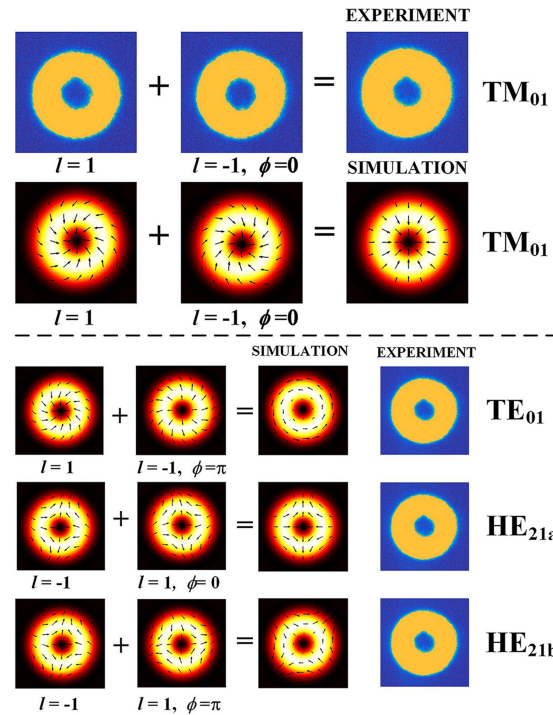
Fig. 3. Experimental and simulated generation of PCVBs. The type of PCVB generated (here: TM_{01}, TE_{01}, even and odd HE_{21}) depends on the specific topological charge (l) and phase difference (ϕ) ascribed to each interfering beams.

with opposite topological charges whose intensity profiles are shown on the first two columns of Fig. 3. The phase masks employed are blazed fork grating structures designed such that the total diffraction efficiency into the first order is maximal. We note that the overall efficiency of the proposed scheme is currently limited to 25% due to the double passage through a beam splitter. Fig. 3 also displays the experimental and simulated beam profiles of the generated PCVBs with the local E-field vectors denoted by arrows in the simulations. For demonstration purposes, we applied the proposed method for the generation of three different types of CVBs: the radial and azimuthally polarized CVBs that are respectively analogous to the TM_{01} and TE_{01} modes of an optical fiber, as well as an in-homogeneously polarized CVB with direct correspondence to the even and odd HE_{21} modes of a fiber. For the latter exemplar set of PCVBs, the relative phase difference between the two interfering beams (set by the phase masks on the SLM) was varied from $\phi = 0$ to $\phi = \pi$, as shown in Fig. 3. Still, we again stress that the proposed method is in fact general since the SLM can be programmed with different phase and topological charges so as to generate any other types of PCVB or perfect vortex beams for that matter, all using the same experimental setup. As indicated earlier and suggested in Fig. 1, the key feature of this work stems from the ability to tailor both the ring diameter and ring width of the PCVB independently from one another. The latter is here accomplished through two "knobs": the axicon parameter (a) and the iris parameter via the input Gaussian beam waist (w_g). The procedure to generate a PCVB is thus divided into two stages. In the first stage, the variable iris is used to control the diameter of the input Gaussian beam, which enables one to tune the ring width (R_W) of the PCVB. As the input beam width (w_g) increases, the ring width decreases in both directions, inward as well as outward. In the second stage, the axicon mask (along with the lens function) imprinted on the SLM allows the independent control of the ring diameter (R_D). The demonstration of PCVB with complete control over the transverse dimensions of the CVB is shown in Fig. 4 for increasing values of the axicon and iris parameters. The ring diameter (R_D) of PCVB was increased or decreased via the axicon parameter (a) for a given fixed input Gaussian beam width.
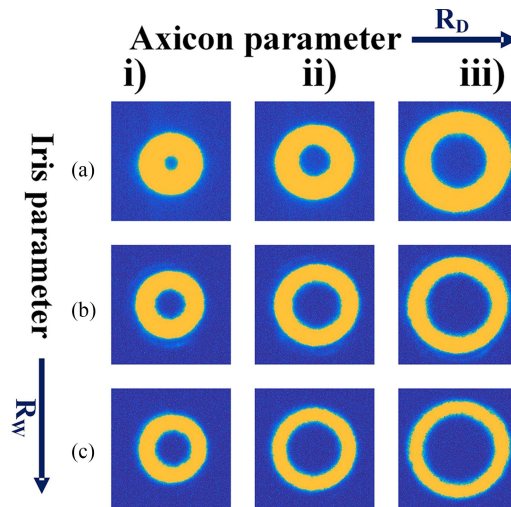
Fig. 4. Experimental demonstration of PCVB (a radially polarized beam was here used). From left to right (i-iii) columns, the ring diameter R_D increases with the axicon parameter. From top to bottom (a-b-c) rows, the ring width R_W decreases with the iris parameter.

TABLE 1

Measured Values of the R_D and R_W on the CCD Camera for Each PCVB Shown in Fig. 4

R_D(mm) / R_W(mm)	i)	ii)	iii)
a)	0.61 / 0.25	0.73 / 0.22	0.87 / 0.21
b)	0.65 / 0.18	0.78 / 0.17	0.93 / 0.17
c)	0.65 / 0.16	0.79 / 0.14	0.93 / 0.14

Table 1 presents the measured values of the ring diameter (R_D) and ring width (R_W) that are shown in Fig. 4. The results indicate an average fluctuation of around 3% for a given constant ring diameter (i.e. along a single column i, ii or iii) while the iris parameter (R_W) is varied. We ascribe this small error to the aperture diffraction incurred when the iris is gradually closed to modify the input beam width. This effect causes a slight reduction in the brightness of the recorded beam, which in turn affects the intensity contrast (i.e. image sharpness) of the recorded beam profile. We note that the ultimate size of ring width possible with this method is only limited in practice by the aperture of the iris utilized (see Fig. 2). However, this iris could be replaced by a lens arrangement (i.e. tunable beam expander) that would extend the input beam diameters possible with this approach. The maximum achievable size of ring diameter is mainly restricted by the aperture stop of the lenses and half wave plate located before the SLM. On the other hand, the minimum size of the ring diameter is limited by the minimum input size of the Gaussian beam. Measurements in Table 1 further indicate that for a given constant ring width (along a single row a, b or c) there is an average error of 5% in the stability of the ring width (R_W) while the ring diameter (R_D) is varied. This small fluctuation stems from the Fourier transformation of the Bessel-Gauss beams as pointed out in [24]. The experimental validation of the kind of PCVB generated was performed with the well-known method of the rotating analyzer (Fig. 5), as described in [1], [26]. The first column in Fig. 5 presents a schematic representation of the E-field vector distribution of the PCVBs of interest. By rotating the linear polarizer in front of the CCD camera (first row) and by simultaneously monitoring the resulting intensity profiles on the camera (subsequent rows), one can deduce the type of PCVB (TM_{01}, TE_{01} and even or odd HE_{21}) at hand. We note that the intensity distributions of the TM_{01} and TE_{01} modes rotate in the same direction while rotating the linear polarizer in front of the CCD camera, whereas the intensity distributions of the even or odd HE_{21} modes rotate in the opposite direction.
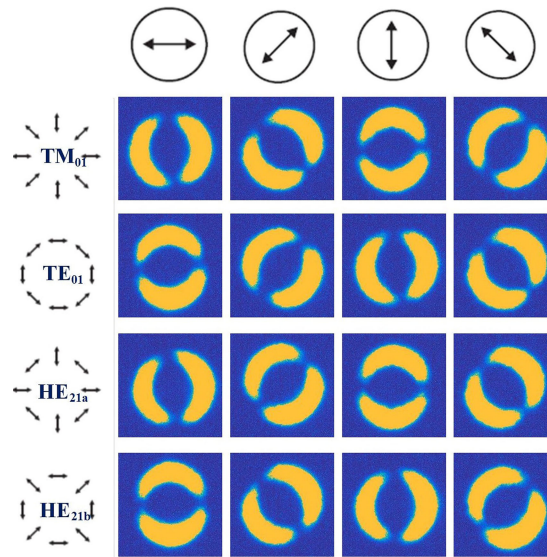
Fig. 5. Experimental identification of the generated PCVBs (TM$_{01}$, TE$_{01}$, even and odd HE$_{21}$ beams) via the rotation of a linear polarizer located in front of the CCD camera.

TABLE 2

Mode Purity Measurement of PCVBs

PCVBs	Simulation (dB)	Experimental (dB)
TE$_{01}$	33.65	19.10
TM$_{01}$	33.65	18.13
HE$_{21,even}$	33.65	18.23
HE$_{21,odd}$	33.65	18.53

To determine the mode purity of the PCVBs generated with this method, the azimuthal intensity distribution of the doughnut shaped intensity profiles was recorded. A calculation based on the visibility of the intensity ring pattern reveals that the PCVBs produced in this work were of high purity ($>$18 dB) as indicated in Table 2. The approach used to determine the mode purity is detailed in Appendix B.

5. Conclusion

We have proposed and demonstrated the generation of high-purity *perfect cylindrical vector beams* (PCVB) whose transverse profile dimensions (i.e. ring width and ring diameter) can be independently controlled using an iris and a diffractive phase mask implemented on a digital spatial light modulator (SLM). Although the work was restricted to the generation of well-known PCVBs (the HE$_{21}$ mode, radially and azimuthally polarized TM$_{01}$ and TE$_{01}$ modes), we emphasize that the proposed method can be directly generalized to any arbitrary PCVB as well as for the generation of perfect vortex beams, using the same experimental setup. The ability to generate PCVBs and tune their dimensions through a digitally addressable SLM obviates the need for the repeated tedious manipulation and re-alignment of bulk optics in the setup. The ensuing perfect cylindrical vector beams and perfect vortex beams are of high topical interest in the areas of laser material processing, super-resolution microscopy, fiber launching of exotic optical states and spin-orbit optical interactions, among others.

Appendix A

The interference of the two perfect vortex beams (of opposite topological charges) leading to the generation of a PCVB with the desired spatial polarization and transverse dimensions, depends on the user-defined phase masks imprinted on the SLM. A given phase mask is here designed by combining an axicon phase, a lens function and a spiral phase function that also implements the appropriate relative phase shift (between the two interfering beams). The resulting complex phase mask is given by [14]:

$$\exp\left(\frac{-ikR^2}{2f} - iaR + il\theta\right) \tag{11}$$

where k denotes the total wavevector, f is the focal length and a the axicon parameter. The first term of (11) represents a lens function while the next term is the axicon function that is used to control the ring diameter (R_D) of the PCVB. The axicon parameter used in this phase mask has a relationship between the radial and total wavevectors defined by

$$a = k\sin^{-1}\left(\frac{k_r}{k}\right) \tag{12}$$

with $k_r = \frac{2.405}{B_o}$ and B_o being the first zero of the zero-order Bessel beam. Finally, the third term of (11) represents a spiral phase function that is used to produce two beams with opposite topological charges ($l = \pm 1$). The practical implementation of this complex phase mask is schematically described in Fig. 6.
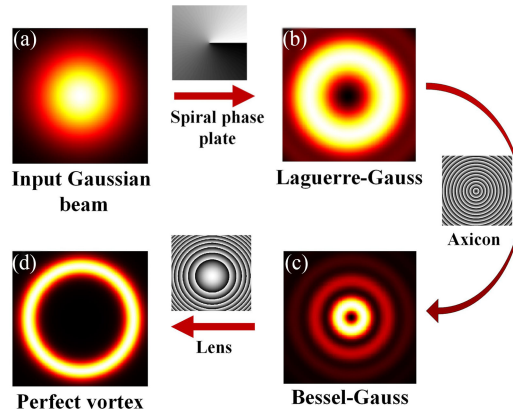

Fig. 6. Simulation of the (a) input Gaussian beam, (b) Laguerre-Gauss beam after passing through the spiral phase function, (c) Bessel-Gauss beam after undergoing the axicon function, and (d) the perfect vortex beam is obtained after the lens function.

Fig. 6 shows the physical procedure for transforming an input Gaussian beam into a PCVB. The input Gaussian beam sequentially passes through the three different stages of the complex phase mask described in (11) that is imprinted on one half-side of the SLM. In the example of Fig. 6, here a right(-left) circularly polarized input Gaussian beam after passing through the spiral phase function yields a Laguerre-Gauss beam of prescribed topological charge ($l = \pm 1$). Next, the beam is transmitted through the axicon function thus generating a Bessel-Gauss beam. Subsequently, the Bessel-Gauss beam is Fourier transformed into a perfect vortex beam after passing through the lens function. The latter procedure is performed on both arms of the common-path interferometric arrangement (but using different phase masks on each half-side of the SLM). Finally, when the two perfect vortex beams of opposite topological charges are made to interfere, the ensuing optical beam forms the desired type of PCVB (TM_{01}, TE_{01} or even and odd HE_{21} modes) as shown in Fig. 3.

Appendix B

To test the quality of the PCVB generated using our experimental setup, we measured the purity of the TM_{01}, TE_{01} or even and odd HE_{21} beams based on the visibility of their intensity pattern given by [27]

$$V = \frac{I_{max} - I_{min}}{I_{max} + I_{min}} \qquad (13)$$

Where I_{max} and I_{min} are the intensity maxima and minima of the beam along the azimuthal intensity distribution. Hence, the mode purity is calculated using

$$Mode\ purity\ (dB) = 10\log_{10}\left(\frac{1+\sqrt{1-V}}{V}\right)^2 \qquad (14)$$

Fig. 7(a) shows the azimuthal intensity distribution along the ring for an ideal TE_{01} mode obtained from simulation. Keeping the simulated result as reference, we then present the azimuthal intensity distribution of the experimentally obtained TE_{01} PCVB as displayed in Fig. 7(b). The beam purity measurements of the TM_{01} and HE_{21} PCVBs were similarly calculated and their values reported in Table 2.
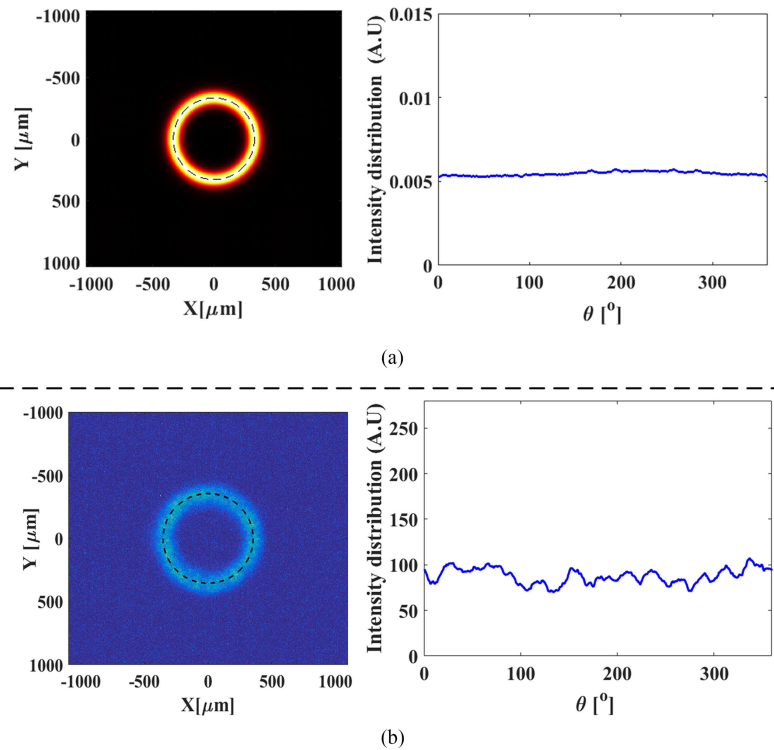

(a)

(b)

Fig. 7. (a) Simulated and (b) experimental TE_{01} PCVB with the centered azimuthal intensity profile recorded along the dashed line. This azimuthal profile is ultimately used to calculate the beam purity.

References

[1] Q. Zhan, "Cylindrical vector beams: From mathematical concepts to applications," *Adv. Opt. Photonics*, vol. 6, no. 1, pp. 1–57, 2009.
[2] A. P. Porfirev, A. V. Ustinov, and S. N. Khonina, "Polarization conversion when focusing cylindrically polarized vortex beams," *Sci. Rep.*, vol. 6, no. 1, 2016, Art. no. 6.

[3] Y. Chen, Z. X. Fang, Y. X. Ren, L. Gong, and R. D. Lu, "Generation and characterization of a perfect vortex beam with a large topological charge through a digital micromirror device," *Appl. Opt.*, vol. 54, no. 27, pp. 8030–8035, 2015.

[4] Z. Bomzon, G. Biener, V. Kleiner, and E. Hasman, "Radially and azimuthally polarized beams generated by space-variant dielectric subwavelength gratings," *Opt. Lett.*, vol. 27, no. 5, pp. 285–287, 2002.

[5] G. Milione *et al.*, "Measuring the self-healing of the spatially inhomogeneous states of polarization of vector Bessel beams," *J. Opt.*, vol. 17, no. 3, 2015, Art. no. 035617.

[6] K. S. Youngworth and T. G. Brown, "Focusing of high numerical aperture cylindrical-vector beam," *Opt. Exp.*, vol. 7, no. 2, pp. 77–87, 2000.

[7] R. Dorn, S. Quabis, and G. Leuchs, "Sharper focus for a radially polarized light beam," *Phys. Rev. Lett.*, vol. 91, no. 23, 2003, Art. no. 233901.

[8] M. Duocastella and C. B. Arnold, "Bessel and annular beams for materials processing," *Laser Photon. Rev.*, vol. 6, no. 5, pp. 607–621, 2012.

[9] Y. Kozawa and S. Sato, "Optical trapping of micrometer-sized dielectric particles by cylindrical vector beams," in *Opt. Exp.*, vol. 18, no. 10, pp. 10828–10833, 2010.

[10] P. Török and P. R. T. Munro, "The use of Gauss-Laguerre vector beams in STED microscopy," *Opt. Exp.*, vol. 12, no. 15, pp. 3605–3617, 2004.

[11] Y. Kozawa and S. Sato, "Numerical analysis of resolution enhancement in laser scanning microscopy using a radially polarized beam," *Opt. Exp.*, vol. 23, no. 3, pp. 2076–2084, 2015.

[12] Y. Wentao *et al.*, "Super-resolution deep imaging with hollow Bessel beam STED microscopy," *Laser Photon. Rev.*, vol. 10, no. 1, pp. 147–152, 2016.

[13] C. Brunet, P. Vaity, Y. Messaddeq, S. LaRochelle, and L. A. Rusch, "Design, fabrication and validation of an OAM fiber supporting 36 states," *Opt. Exp.*, vol. 22, no. 21, pp. 26117–26127, 2014.

[14] P. Vaity, C. Brunet, Y. Messaddeq, S. LaRochelle, and L. A. Rusch, "Exciting OAM modes in annular-core fibers via perfect OAM beams," in *Proc. Eur. Conf. Opt. Commun.*, 2014, pp. 1–3.

[15] M. Chen, M. Mazilu, Y. Arita, E. M. Wright, and K. Dholakia, "Dynamics of microparticles trapped in a perfect vortex beam," *Opt. Lett.*, vol. 38, no. 22, pp. 4919–4922, 2013.

[16] A. S. Ostrovsky, C. R. Parrao, and V. Arrizón, "Generation of the perfect optical vortex using a liquid-crystal spatial light modulator," *Opt. Lett.*, vol. 38, no. 4, pp. 534–536, 2013.

[17] P. Li *et al.*, "Generation of perfect vectorial vortex beams," *Opt. Lett.*, vol. 41, no. 10, pp. 2205–2208, 2016.

[18] H. Ma *et al.*, "In situ measurement of the topological charge of a perfect vortex using the phase shift method," *Opt. Lett.*, vol. 42, no. 1, pp. 135–138, 2017.

[19] M. V. Jabir, N. A. Chaitanya, A. Aadhi, and G. K. Samanta, "Generation of perfect vortex of variable size and its effect in angular spectrum of the down-converted photons," *Sci. Rep.*, vol. 6, no. 1, 2016, Art. no. 21877.

[20] S. Fu, T. Wang, and C. Gao, "Generating perfect polarization vortices through encoding liquid-crystal display devices," *Appl. Opt.*, vol. 55, no. 23, pp. 6501–6505, 2016.

[21] M. K. Karahroudi, B. Parmoon, M. Qasemi, A. Mobashery, and H. Saghafifar, "Generation of perfect optical vortices using a Bessel–Gaussian beam diffracted by curved fork grating," *Appl. Opt.*, vol. 56, no. 21, pp. 5817–5823, 2017.

[22] Y. Liu *et al.*, "Generation of perfect vortex and vector beams based on Pancharatnam-Berry phase elements," *Sci. Rep.*, vol. 7, 2017, Art. no. 44096.

[23] T. Wang, S. Fu, F. He, and C. Gao, "Generation of perfect polarization vortices using combined gratings in a single spatial light modulator," *Appl. Opt.*, vol. 56, no. 27, pp. 7567–7571, 2017.

[24] P. Vaity and L. Rusch, "Perfect vortex beam: Fourier transformation of a Bessel beam," *Opt. Lett.*, vol. 40, no. 4, pp. 597–600, 2015.

[25] C. Maurer, A. Jesacher, S. Fürhapter, S. Bernet, and M. Ritsch-Marte, "Generation of perfect vortex of variable size and its effect in angular spectrum of the down-converted photons," *New. J. Phys.*, vol. 9, no. 3, 2007, Art. no. 78.

[26] P. Pradhan, D. Sengupta, L. Wang, C. Tremblay, S. LaRochelle, and B. Ung, "The Brillouin gain of vector modes in a few-mode fiber," *Sci. Rep.*, vol. 7, 2017, Art. no. 1552.

[27] N. Bozinovic, P. Kristensen, and S. Ramachandran, "Long-range fiber-transmission of photons with orbital angular momentum," in *Proc. Conf. Lasers Electro-Opt.*, 2011, pp. 1–2.